

Structural determinants of DNA recognition by the NO sensor NsrR and related Rrf2-type [FeS]-transcription factors

Roman Rohac¹, Jason C. Crack², Eve de Rosny ¹, Océane Gigarel¹, Nick E. Le Brun ², Juan C. Fontecilla-Camps¹ & Anne Volbeda ¹✉

Several transcription factors of the Rrf2 family use an iron-sulfur cluster to regulate DNA binding through effectors such as nitric oxide (NO), cellular redox status and iron levels. [4Fe-4S]-NsrR from *Streptomyces coelicolor* (ScNsrR) modulates expression of three different genes via reaction and complex formation with variable amounts of NO, which results in detoxification of this gas. Here, we report the crystal structure of ScNsrR complexed with an *hmpA1* gene operator fragment and compare it with those previously reported for [2Fe-2S]-RsrR/*rsrR* and apo-IscR/*hyA* complexes. Important structural differences reside in the variation of the DNA minor and major groove widths. In addition, different DNA curvatures and different interactions with the protein sensors are observed. We also report studies of NsrR binding to four *hmpA1* variants, which indicate that flexibility in the central region is not a key binding determinant. Our study explores the promotor binding specificities of three closely related transcriptional regulators.

¹Univ. Grenoble Alpes, CEA, CNRS, Institut de Biologie Structurale, Metalloproteins Unit, F-38000 Grenoble, France. ²Centre for Molecular and Structural Biochemistry, School of Chemistry, University of East Anglia, Norwich Research Park, Norwich NR4 7TJ, UK. ✉email: anne.volbeda@ibs.fr

All microorganisms need to rapidly sense environmental changes and to respond to them in order to survive, adapt and reproduce. This response is mainly mediated by transcription factors (TFs) that regulate the expression of relevant proteins by either blocking or favoring the activity of RNA polymerases at specific gene sites^{1,2}. Besides their cognate DNA-binding site region, TFs generally have a domain that recognizes effectors, such as other proteins or small ligands. Members of the CRP-FNR and Rrf2 families of dimeric microbial TFs can use the gas-binding affinity, redox properties and intrinsic lability of iron-sulfur clusters to modulate their DNA binding^{3–7}. The well-studied Fumarate Nitrate Reductase regulator (FNR) uses a [4Fe-4S] cluster to sense O₂ levels and to regulate a dimer ↔ monomer transition mediated by cluster disassembly and a metastable protein interface⁸. Only the dimer binds to specific DNA sites⁹. The Rrf2 family was first described in *Desulfovibrio vulgaris* Hildenborough¹⁰ and the three-dimensional structure of the cysteine metabolic regulator CymR from *Bacillus subtilis* (Bs), which does not bind an iron-sulfur cluster, was the first to be reported for a member of this family¹¹. Structural and functional studies of the related *Staphylococcus aureus* (Sa) CymR revealed a sensing mechanism in which DNA binding is lost under oxidative stress conditions after oxidation of a surface cysteine thiol¹². BsCymR binds to DNA after forming a complex with O-acetylthiol-lyase only when cysteine is present¹³.

Members of the Rrf2 family that coordinate iron-sulfur clusters use them to sense various effectors and regulate gene expression to enable adaptation, maintenance of homeostasis and cell protection. Characterized cluster-binding TFs include: IscR from *Escherichia coli* (Ec) and *Thermotoga lotus* (Tl) that sense cell iron-sulfur cluster levels and oxidative stress^{6,14}; RsrR, a redox-sensitive response regulator from the soil bacterium *Streptomyces venezuelae* (Sv)⁵; *Rhizobium leguminosarum* (Rl) RirA that uses a labile [4Fe-4S] cluster to regulate cellular iron concentrations¹⁵; and NsrR, a regulator of nitric oxide (NO)-induced stress in many bacterial species^{4,16}. The regulation of their DNA binding capabilities depends on protein conformational changes caused by the status of the cluster or its absence. The first crystal structures of an iron-sulfur sensor of the Rrf2 family were those of the apo-form of Ec- and Tl-IscR^{17,18}. More relevant to the work reported here, the structure of apo-EcIscR in complex with a

29 base pair (bp) fragment of the hydrogenase-1 *hyA* operator was also solved¹⁷. The structure of [2Fe-2S]-IscR, which recognizes different operator sequences¹⁹, has not yet been determined, either alone or in complex with DNA.

We have reported the crystal structures of [2Fe-2S]-SvRsrR alone²⁰ and in complex with cognate DNA, the latter at medium resolution²¹. Using a combined approach of structural and mass spectrometric studies and molecular dynamics calculations, we were able to show how the one-electron cluster reduction of [2Fe-2S]-SvRsrR triggers protonation of a histidine residue and the burial of a tryptophan side chain, causing conformational changes that lead to DNA dissociation²¹. Our groups have also reported the holo- and apo- crystal structures of NsrR from the antibiotic-producing bacterium *Streptomyces coelicolor* (Sc)²². The principal regulatory target of this TF is, in most organisms, the *hmp* gene, which encodes a flavohemoglobin that converts NO to nitrate (NO₃⁻) or nitrous oxide (N₂O) under aerobic or anaerobic conditions, respectively^{23,24}.

ScNsrR is so far the only NsrR to have been characterized in significant detail^{22,24–28}. Its regulon is small, enabling a detailed investigation of the relative DNA binding properties of [4Fe-4S]-ScNsrR to each identified operator: *hmpA1*, *hmpA2*, and *nsrR*, showing a 23-base pair (bp) consensus recognition site. Tightest binding was observed for *hmpA1*, followed by *nsrR* and *hmpA2*.²⁵ In the presence of NO, the ScNsrR [4Fe-4S] cluster is rapidly lost, causing the dissociation of the protein-DNA complex. Binding of *hmpA2* was found to be the most sensitive to NO, followed by *hmpA1* and *nsrR*²⁴. Apo-ScNsrR (or [2Fe-2S]-ScNsrR, which could be generated and stabilized upon O₂ exposure in the presence of β-mercaptoethanol²⁹) did not bind DNA with significant affinity²⁵. In some bacteria, such as Ec and *Salmonella enterica* serovar Typhimurium, many more genes are under NsrR control, suggesting a broader regulatory role for NsrR in these microorganisms^{30,31}.

A comparison of the three-dimensional structures of holo [4Fe-4S]-ScNsrR and apo-ScNsrR furnished a first model to understand how NO binding to the iron-sulfur cluster, and the resulting conformational changes, control the configuration of the protein DNA-binding surface²². Here, we report the 3.0 Å resolution X-ray structure of ScNsrR complexed with a 23-bp *hmpA1* operator fragment and use it, alongside the structures referred to above, to establish what determines the DNA binding specificity among the three structurally-related iron-sulfur Rrf2 family proteins IscR, RsrR and NsrR. DNA recognition is generally considered to depend on either a direct readout of the nucleobase sequence, a readout of a sequence-dependent DNA phosphate backbone shape, or a combination thereof^{32,33}. Related to the recognition process is the flexibility of the DNA operator regions and their propensity to undergo conformational changes upon protein binding. In a classical study³⁴, a crystalline B-DNA dodecamer went from an almost straight double helix structure to a bent one as the temperature was changed from 7 °C to 20 °C. DNA flexibility has also been shown by solution NMR studies: the ³¹P chemical shifts of double stranded (ds) B-DNA fragments vary as a function of the sequence-dependent ratio of B_I and B_{II} backbone states. These are in a dynamic conformational equilibrium, with B_I being the most commonly observed in regular B-DNA³⁵. We have explored these aspects by comparing the remarkably different DNA binding modes of [4Fe-4S]-ScNsrR (this work), apo-IscR¹⁷ and [2Fe-2S]-RsrR²¹ in their respective crystal structures. In addition, we have tested four modified oligonucleotides sequences between two recognition sites of the NsrR regulator in order to explore the effect of DNA flexibility on its binding. This analysis allows us to propose a series of structural features that determine specific DNA binding within a class of closely related proteins.

Table 1 X-ray data collection and refinement statistics.

X-ray data		Refinement	
Space group	P6 ₅	Resolution (Å)	51.45–3.00
Cell dimensions		Reflections	13678/716
		(work/free)	
a = b, c (Å)	118.8 89.5	R _{work} /R _{free}	22.0/23.9
α = β, γ (°)	90 120	Number of atoms	3114
Resolution (Å) ^a	67.54–3.0	Protein	2151
	(3.18–3.0)		
best in h k plane	3.14	DNA	943
best along l axis	3.00	[4Fe-4S] cluster	16
R _{sym} (%)	5.9 (194.5)	Water	4
Mean(I/σ(I))	12.6 (1.0)	Average B factors (Å ²)	
		Protein	134.2
CC(1/2)	0.999 (0.516)	DNA	181.4
Completeness (%)	99.8 (100.0)	[4Fe-4S] cluster	110.7
Redundancy	6.3 (6.7)	Water	118.1
		R.m.s. deviations	
		Bond lengths (Å)	0.003
		Bond angles (°)	0.70

^aValues within parentheses denote the highest resolution shell.

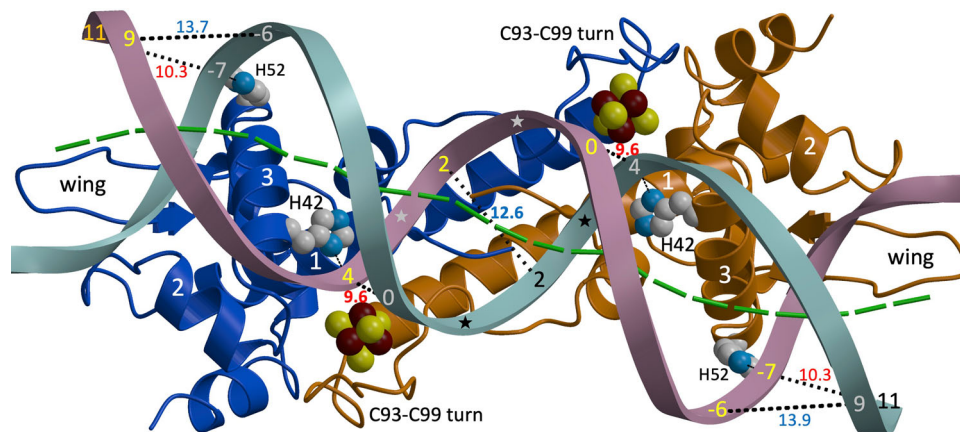


Fig. 1 Top view of the ScNsrR/hmpA1 operator complex. NsrR subunits C α tracings are depicted in blue and gold with ribbons indicating α -helices and arrows β -strands. DNA strands carry nucleotide numbers and are shown as cyan and burgundy ribbons, with stars marking four B_{II} backbone conformations in the central region. Cluster atoms and histidine side chains forming hydrogen bonds to phosphate groups are depicted as spheres (Fe: red-brown, S: yellow, N: blue and C: gray). The first three helices and the labeled wing loop of each protein subunit interact with the DNA. Minimal and maximal P-to-P distances between phosphate groups across the minor groove are indicated with dotted lines and given in Å. The green dashed line follows the bp origins of the DNA double helix as determined with the program DSSR³⁷.

Results

Structure of the [4Fe-4S]-ScNsrR-hmpA1 operator complex.

Table 1 shows the statistics of the 3.0 Å resolution structure of [4Fe-4S]-ScNsrR complexed to the 23-bp *hmpA1* operator fragment. High atomic temperature (B) factors indicate significant disorder, in agreement with the flexible and dynamic structure previously observed for the noncomplexed protein structure²². Both the operator fragment and the bound protein dimer are about 80 Å long (Fig. 1). The buried surface area (BSA) of the protein/DNA complex is 4222 Å², comparable to the BSA of 4981 Å² of the NsrR dimer but much larger than the 1996 Å² buried between the two strands of the DNA helical fragment. The BSA at the protein/DNA interface of the *Ecl*ScR/*hyA* complex¹⁷ is 3780 Å². This relatively low value is explained by the fact that some of the amino acids of *Ecl*ScR facing the central region of the *hyA* operator were not resolved and therefore not included in the structure. A higher value of 4490 Å² is obtained for the *Sv*RsrR/*rsrR* complex²¹ because the larger 39 bp *rsrR* operator fragment covers the protein sensor more extensively than the 23 bp *hmpA1* one does.

Residues 59–64 of the ScNsrR dimer wings, which are disordered in the free protein²², are partially resolved in the complex where they interact with the ends of the *hmpA1* operator fragment (Fig. 1). Other DNA binding regions include the N-termini of α -helices 1 and 2 and the side of the third one, which corresponds to the regulatory helix (RH) of a helix-turn-helix (HTH) motif. Conversely, the C93–C99 turn, which we previously considered as a potential additional contact interface²², does not directly interact with the DNA. Compared to many other proteins with a winged (w) HTH motif³⁶, the DNA binding region of ScNsrR contains an additional preceding α -helix and, consequently, can be better described as an H-wHTH motif.

Structure of the DNA *hmpA1* fragment. The 23 bp *hmpA1* operator fragment has a B-DNA conformation. The double helix runs almost straight through the central 11 bp region and bends at its extremes around α -helix 3 of each of the NsrR subunits (Fig. 1). The distance between phosphate P atoms across the minor groove (MiG) decreases from 12.6 Å at the center of the fragment to 9.6 Å between nucleotides 0 and +4 of the other strand. It increases again to about 13.8 Å between nucleotides +9 and –6 before narrowing to 10.3 Å between nucleotides +11

and –7. Minimal MiG distances are observed for the +4 and –7 phosphates, which respectively interact with the His42 and His52 imidazole groups. An analysis of torsion angles with the program DSSR³⁷ (Fig. S1) shows that 32 of the 44 phosphate groups in the bound 23 bp *hmpA1* operator fragment (excluding the 5'-terminal ones) are in the B_I conformation. Conversely, the phosphates bound to the C3' atom of the 0 and +2 nucleotides are in the B_{II} conformation (see also Fig. S2), while the remaining ones are in a conformation intermediate between B_I and B_{II} (Fig. 2). The reorientation of the T₊₂ 3'-phosphates from B_I to B_{II} conformations causes propeller twists of –19.0° for bp C_{+3c}/G_{-3d} (Figs. 3 and S3) and –15.9° for bp T_{-3c}/A_{+3d}.

Protein-DNA interactions. Most of the ScNsrR contacts are made with the phosphate backbone of the *hmpA1* operator (Figs. 2, 3 and Table S1). The His42-N δ 1 and His52-N ϵ 2 atoms interact with the respective 5'-phosphate groups of nucleotides +4 and –7 in opposite strands (Figs. 1–3). These interactions could be salt bridges if the N δ 1 and N ϵ 2 atoms of the imidazole groups are protonated. The side chains of Arg2, Lys5 and Lys45, present at the contact interface, are disordered (Fig. S4), as they were in the 1.95 Å resolution structure of non-complexed [4Fe-4S]-ScNsrR²². However, these basic residues could still interact with the negatively charged DNA phosphate backbone (Fig. S5). The positive dipole moments at the N-termini of α -helices 1 and 2 provide additional electrostatic stabilization via H-bonds from: (i) Lys5 main chain N atom to OP1 and Phe6-N to OP2 of the 5'-phosphate group of the +3 nucleotide, which is in a B_{II} conformation (the non-complexed ScNsrR structure has a bound sulfate at this position, see Fig. S6); (ii) Thr29 main chain N atom to the 5'-phosphate of the –9 nucleotide in the opposite strand, which is also hydrogen bonded to Thr29-O γ 1. The Thr41 and Thr48 O γ 1 atoms of α -helix 3 make similar H-bonds to the respective 5'-phosphates of the +5 and –8 nucleotides in opposite strands.

There are only a few specific interactions between ScNsrR amino acid side chains and the nucleobases of the *hmpA1* operator (Fig. 3 and Table S1). In the major groove (MaG), Lys45 could establish H-bonds to ring atoms of G₋₆ and surrounding bases. However, its weak electron density (Fig. S4) makes a definite assignment difficult. The 58–61 and 66 wing residues bind edge-on to the MiG (see also Fig. S3b), with Arg60 making the most contacts to the DNA. These include a H-bond between

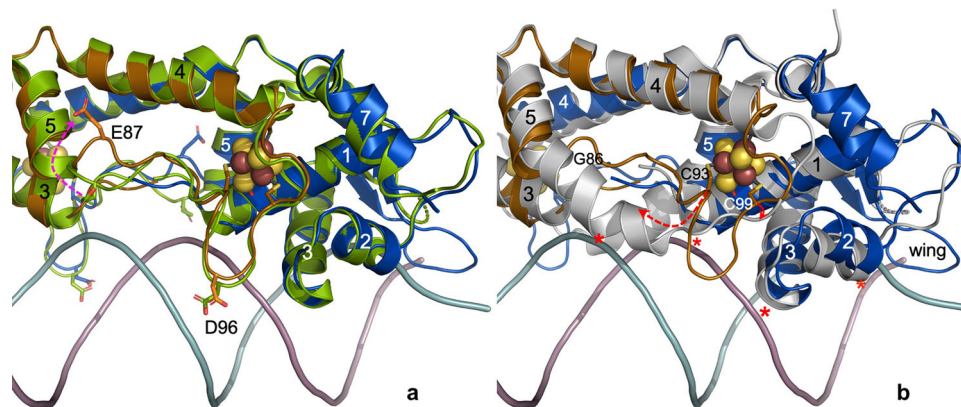


Fig. 4 Comparison of [4Fe-4S]-ScNsrR/hmpA1 complex with DNA-free structures. **a** Structural superposition of the complex to [4Fe-4S]-ScNsrR (green, cluster not shown). **b** Superposition to apo-3CA-ScNsrR (gray). The complex is colored as in Fig. 1 and selected amino acid residues are highlighted. Red arrows indicate movements observed for residues 87, 93 and 99. Regions of the apo structure that would collide with *hmpA1* are indicated by red asterisks. Atom color codes are as in Fig. 3. Rotated stereo zooms of the same superpositions are given in Fig. S6 and S8.

	===== α 1=====	===== α 2====	===== α 3=====	β A>-wing-- β B>	%ID	pdcb
ScNsrR	1MrLTkftd1ALrslmrLAvvrdgdePlat	urevAEvvGvpythaaKai	urLqhlGvVear	RGRgGGltLt	69	7BOC
EcNsrR	1MqLTsftdYGLraliymAslpe-grmtS	isevtdvyGV	SrmhmvKiinq	LsrAGyVtaVRGknGGirLG	68	40
RIRirA	1MrLTkqtnYAvrmlmycAandG--hls	ripeIArrayGV	SelfLfKilqp	LnkAGLVetVRGrnGGvrLG	67	39
SvRsrR	1MKLSggvewALccvvLtaa---srPvp	aarlaELhdV	SpsyLaKqma	LsrAGLVrsvGktGGYvLT	66	30 6Y42
EcIscR	1MrLTSKGrYAvtaMldvAlnsea-GPvp	IadIsErqGiSl	SYLEQLfsr	LrknGLVsVRGpgGGYlLG	68	28 4HF1
TpIscR	3lKvStKGhYGVqamFdLAqhfGe-GPv	SLksIAErqG	SepYLEQLiav	LrkAGLVkSVRGaqGGYiLA	68	22 4CIC
SaCymR	1MKiStKGrYGLtlMisLakkeGq-G	iSLksIAEennl	SdlyLEQLvqp	LrnAGLirSVRGakGGYqLr	68	19 3T8R
BsCymR	2lKiStKGrYGLtiMieLakkhGe-GPt	SLksIAqtnnl	SehYLEQLvsp	LrnAGLVkSiRGayGGYvLG	69	19 2Y75

Fig. 5 H-WTH motif sequence alignment of eight selected Rrf2 family members. Numbered α -helices (H) and labeled wing β -strands are shown on top for ScNsrR; residues conserved in at least four sequences are indicated with capitals and given in bold when they are invariant. Percentages of sequence identity with ScNsrR and Protein Data Bank codes for the structures used here are given in the %ID and pdcb columns, respectively. Residues with H-bond or salt bridge distances ≤ 3.3 Å to phosphate groups in the ScNsrR/hmpA1, SvRsr/rsr and EcIscR/hyA structures are highlighted in orange and those that form H-bonds to nucleobases are depicted in turquoise; additional residues within 3.8 Å of the bound DNA fragments are highlighted in gray and those that are different from ScNsrR are shown in red. Cluster binding residues in ScNsrR and SvRsrR and the oxidation-sensitive cysteine of SaCymR are highlighted in purple. Abbreviations for different bacteria are defined in the text. *Tp*, *Sa*, and *Bs* are Gram-positive bacteria, all the others are Gram-negative.

Comparison with other sensors of the Rrf2 family. The homologous *E. coli* NO sensor displays several amino acid sequence differences with ScNsrR in the DNA contacting region (Fig. 5). For example, ScNsrR Thr29, Thr41 and Thr48, which are hydrogen-bonded to phosphate groups of *hmpA1*, are neither conserved in EcNsrR, nor replaced by Ser, which would allow a similar interaction. In addition, the phosphate-binding His52 is substituted by Arg. These dissimilarities could explain why ScNsrR does not display significant affinity for EcNsrR-specific DNA sequences²⁵. The above mentioned His and Thr residues are also not conserved in SvRsrR or EcIscR, the other two Rrf2 family iron-sulfur cluster binding sensors with known DNA complex structures, although Thr41 is replaced here by Ser. His42, the other ScNsrR residue that possibly makes a salt bridge with the phosphate backbone, is replaced by Tyr in those sensors. Amino acid sequence comparisons, including RIRirA and Sa and BsCymR, reveal a conserved Lx₃Gx₆Gx₂GGx₂L motif (Fig. 5) that spans the C-terminal region of helix 3 and the wing region. The comparison shows that most of the ScNsrR DNA contacting residues are not conserved in the eight Rrf2 family members. This indicates, as might be expected, that the different binding modes observed for these sensor/DNA complexes result from a combination of specific amino acid (Fig. 5) and nucleotide (Table 2) differences. A detailed comparison of the ScNsrR/hmpA1 and EcIscR/hyA complex structures reveals a small number of base-specific interactions (Table S1). Modelling different operator sequences on the structures of hmpA1 and hyA produces vdW collisions with the respective ScNsrR and EcIscR protein structures (shown in **bold italics** in Table 2).

DNA operator fragments conformations. The DNA double helices of the 39-bp *rsrR*, 29-bp *hyA* and 23-bp *hmpA1* operator fragments display different shapes in their respective complexes to SvRsrR, EcIscR and ScNsrR (Fig. 6). The DNA structures accommodate the different positions and orientations of the H-WTH motifs found in the bound proteins (Fig. S9). The MiG and MaG P-to-P distances (Fig. 6b, c) and widths (Fig. S10) observed at different locations of the DNA double helix in the three complexes are remarkably different. The MiGs are especially different in the central 7-bp region (Fig. 6b, c) for which no base-specific contacts with the protein are observed (Fig. 2 and Table S1). These groove width variations condition the distance between equivalent operator regions (Fig. S11), which could guide recognition by different Tfs^{32,33}.

To investigate whether the sequence of the central 7-bp region of *hmpA1* is important for DNA recognition by ScNsrR we performed EMSA binding studies of fragments with modified bases (Fig. 7), embedding the 23-bp consensus central region in 151-bp dsDNA probes (see Methods). Wild type *hmpA1* (Av003) has four dinucleotides in a B_{II} phosphate backbone conformation in the 7-bp central region: C_{0c}A_{+1c}, T_{+2c}C_{+3c}, G_{0d}A_{+1d} and T_{+2d}A_{+3d} (Figs. 1–2 and 6). Because XT dinucleotides have a low probability of being in the B_{II} conformation in regular B-DNA³⁸, we replaced A_{+1c} and A_{+1d} by T in probe Av004 and C_{+3c} and A_{+3d} by T in Av005 (see Table S2). The observation that some XT steps are found at the corresponding positions in the aligned *hyA* and *rsrR* operator fragments (Fig. 6a) suggested to us that they could play a discriminating role in DNA recognition between

Table 2 NsrR and IscR base specificity for different operator fragments*.

base	<i>hmpA1</i>	d (Å)	ScNsrR	<i>hyA</i>	d (Å)	<i>rsrR</i>	d (Å)	<i>hyA</i>	d (Å)	EclsrR	<i>hmpA1</i>	d (Å)	<i>rsrR</i>	d (Å)
-10c	A-N3	3.0	R _{60A} O	A-N3	3.0	C-O2	2.8							
-10d	A-N3	3.0	R _{60B} O	A-N3	3.0	C-O2	2.8							
-8c								C-N4	2.7	E _{43B} Oε2	A-N7	3.1	C-N4	2.7
-8d								C-N4	2.8	E _{43A} Oε2	T-C7	2.5	C-N4	2.8
+4c	T-C7	3.5	H _{42B} Cδ2	T-C7	3.6	G		T-O4	3.2	Q _{44A} Nε2	T-O4	3.2	G	
+4d	T-C7	3.6	H _{42A} Cδ2	T-C7	3.6	A		T-O4	3.0	Q _{44B} Nε2	T-O4	3.0	A	
+5c	A-C8	3.6	T _{41B} Oγ1	A-C8	3.6	T-C7	2.9	A-N7	2.9	S _{40A} Oγ	A-N7	2.9	T-C7	1.8
+5d	T-C7	3.6	T _{41A} Cβ	G-C8	3.9	T-C7	3.6	G-N7	2.7	S _{40B} Oγ	T-C7	1.8	T-C7	1.8
+5c								A-N7	3.4	S _{40A} Cβ			T-C7	1.6
+5d								G-N7	3.2	S _{40B} Cβ	T-C7	1.5	T-C7	1.5
+6c	C		T _{41B} Cγ2	T-C7	2.7	C								
+6d	C		T _{41A} Cγ2	T-C7	2.7	C								
+10c	T-O2	3.4	R _{60B} Cδ	T-O2	3.4	G-N2	2.5	T-O2	3.3	R _{59A} Nη2	T-O2	3.3	G-N3	3.4
+10d	T-O2	3.3	R _{60A} Cδ	T-O2	3.3	G-N2	2.2	T-O2	3.5	R _{59B} Nη2	T-O2	3.5	G-N3	3.6

*These are modeled on the known structures of *hmpA1* and *hyA* complexed with ScNsrR and EclsrR. For repulsive interactions the contact distance (d) and corresponding base substitution are in bold italics.

NsrR, IscR and RsrR. However, our EMSA results did not show any clear difference in binding affinity to ScNsrR between the two constructs having XT steps (Av004 & Av005) and the unmodified *hmpA1* (Av003) sequence (Fig. 7a–c). We also checked the binding of variants with an AT-rich (Av006) and a GC-rich (Av007) central region (Fig. 7d–e), because AT-rich base sequences have been associated with an increased likelihood of MiG narrowing³², as observed in the central region of the 23-bp *hmpA1* fragment (Figs. 2 and 6). However, again our results showed that ScNsrR binds the modified operators essentially stoichiometrically and we could detect no significant differences in binding affinities under these conditions. It should be noted that variations in the flexibility of the central region caused by A/T or G/C enrichments^{39–41} could affect DNA-protein binding kinetics. However, such an effect would not be detected by the EMSA assay reported here.

Discussion

In spite of the large buried complex surface, most of the ScNsrR contacts with the *hmpA1* operator are with the phosphate/sugar backbone; only a few direct interactions with nucleobase rings are observed (Figs. 2 and 3). What, then, determines the *hmpA1* specificity for ScNsrR? Like most other DNA-binding proteins, sensors such as NsrR must locate specific targets in order to perform their biological role. Experiments performed with green fluorescent protein (GFP)-tagged *lac* repressor showed it to diffuse along the helical axis of the DNA probe via a sliding mechanism⁴². Furthermore, a similar study using an RNA polymerase demonstrated that this protein tracked the helical pitch along a DNA groove⁴³. These interactions, made of non-specific electrostatic contacts of protein residues with the phosphate backbone, are dominated by a fully entropic potential⁴⁴. Indeed, the electrostatic potential at the ScNsrR surface is consistent with such non-specific interactions playing an important role in DNA recognition (Fig. S5). Specific binding will then require a unique DNA sequence and protein-nucleobases interactions conditioned by the *shape* of both partners⁴⁵.

The shape of B-DNA is determined by sequence-dependent variations in minor and major groove width and curvature that are at least partially coupled. Inter bp rolls, defined as rotations around the base pairing axis perpendicular to the double helix axis, are major contributors to DNA curvature^{46,47}; zero rolls give straight B-DNA double helices⁴⁸. The *hyA* central 11-bp region is curved, as reflected by an average bp roll of 2.3° (Fig. S1). This

value is only 0.5° in *hmpA1*, in which the same region is almost straight. This may be related to the observed presence of four B_{II} backbone conformations in *hmpA1* (Fig. 2). Dinucleotide bps, such as TpC•GpA, with both connecting phosphates in a B_I conformation (i.e., B_I•B_I) are mostly associated with positive rolls, whereas negative rolls are typically found for B_I•B_{II} conformations⁴⁹. As a result, the rolls of a sequence of bps with alternating B_I•B_{II} and B_I•B_I phosphates (like in *hmpA1*) may partially cancel out, producing a smaller average roll than a sequence lacking B_{II} conformations (like in *hyA*). However, our EMSA DNA binding studies (Fig. 7) do not suggest any role, at least in vitro, for the observed B_{II} backbone conformations in *hmpA1* binding to the protein sensor.

Different backbone torsion angle combinations are required for successive dinucleotides to bend in the same direction along the DNA double helix. Factors such as base orientation and stacking, and electrostatic interactions between phosphate groups may influence the torsion angle values. DNA bending towards the MiG, which narrows it, is energetically more costly than its bending towards the MaG⁵⁰. However, the electrostatic repulsion between MiG opposing phosphate groups is greatly reduced by the proximity of positively charged amino acid sidechains. Thus, a minimal MiG width (MiGW) is observed at the +4 phosphate of *hmpA1* and at the +2 phosphate of *hyA*, which respectively make salt bridges with ScNsrR His42 (assuming it is positively charged) and EclsrR Arg2 (Fig. 6). Narrow MiGs in naked DNA have been associated with A/T bp-rich sequences^{32,46}. Stella and coworkers found that the A/T-rich central region of the Fis protein high-affinity DNA binding sites displayed a small MiGW⁴⁶. G/C substitutions in this region increased the MiGW and resulted in lower DNA binding affinity, an effect these authors explained by the increased conformational cost of compressing the MiG. However, B-DNA sequences are known to form dynamically heterogeneous structures that explore a large conformational space⁵¹. When we performed an EMSA binding study of a variant of *hmpA1* with 7 G/C bps in the central region, we did not observe a change in binding affinity to ScNsrR (Fig. 7). Neither did we see an effect when the region was enriched in A/T bps. This may imply that the flexibility of the *hmpA1* DNA central region of the structure does not have a marked effect on the thermodynamics of the recognition of the operator -through either induced fit or conformational selection- by the different shapes and electrostatic potentials at the ScNsrR surface. A possibly kinetic effect would not be detected in the EMSA.

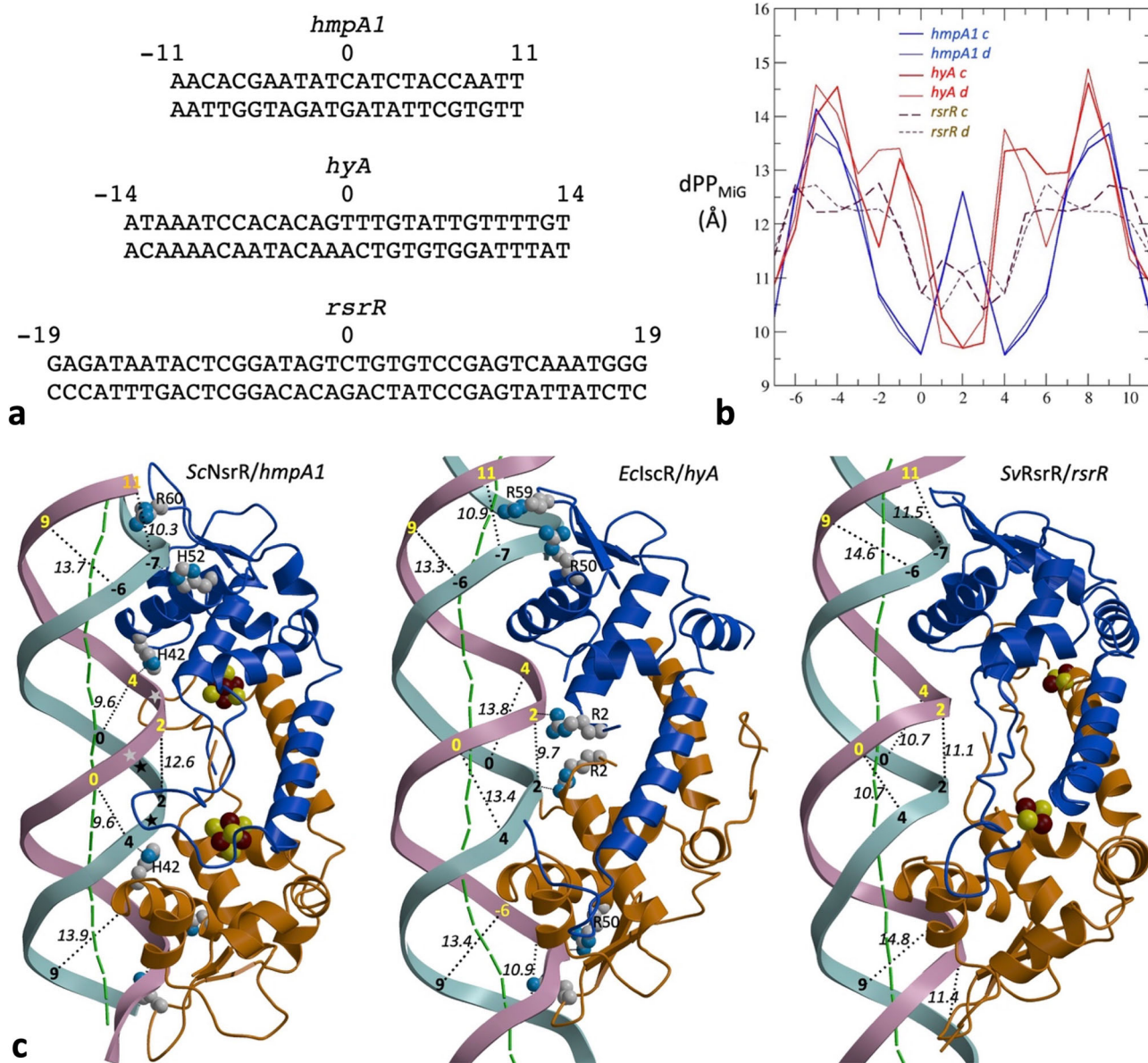


Fig. 6 Shape comparison of the DNA complexes of three Rrf2 family members. **a** Base sequence alignment of *hmpA1*, *hyA* and *rsrR* operator fragments in their corresponding complexes with [4Fe-4S]-ScNsrR, apo-EclscR and [2Fe-2S]-SvRsrR. **b** Comparison of P-to-P distances (dPP_{MiG}) in the MiGs of *hmpA1*, *hyA* and *rsrR* for the phosphate groups in both DNA strands. **c** Polypeptide and DNA folding of the three labeled complexes in a view perpendicular to that of Fig. 1. Protein subunits, DNA strands and bp tracing, phosphate positions, cluster atoms and amino acids are represented as in Fig. 1. Black dotted lines trace dPP_{MiG} distances (given in Å). Because of its limited resolution, no protein residues are shown for the SvRsrR-DNA complex.

In view of these results, *direct* protein-to-DNA interactions, which mostly involve the RH and the wing (Figs. 2 and 6), are probably much more important for operator recognition. The DNA segments bending around the regulatory helix display a widening of the MaG. This widening is more pronounced in *hyA* than in *hmpA1* and *rsrR* (Fig. S10), which could be due to the compression of the MiG between the P_{+2} phosphates of the neighboring central region in *hyA* (Fig. 6). The wing regions of ScNsrR, EclscR and SvRsrR, which display the highest amino acid sequence homologies within Rrf2 family proteins (Fig. 5), interact with a more similar, relatively A/T-rich MiG (Figs. 2 and 6a). In *hmpA1*, as in *hyA*, the corresponding MiGWs are narrower than in *rsrR*. This is probably due to the close interaction of the positively charged ScNsrR Arg60, and EclscR Arg59, with deoxyriboses and base rings at the MiG edge (Fig. 6c and Table S1). These interactions also compensate for the electrostatic repulsion

between opposing phosphate groups. The broader *rsrR* MiG in the region that binds the protein wing could be explained by its lower A/T bp content and by the fact that in SvRsrR this Arg residue is substituted by Gln57 (Fig. 5).

To further analyze DNA binding specificity, we modeled the *hyA* and *rsrR* operator sequences (Fig. 6a) on that of *hmpA1* in its complex with ScNsrR. Substituting *hmpA1* C_{+6} by (*hyA*) T_{+6} introduces a vdW ($d = 2.7$ Å) collision between the added C7 methyl group and the C γ 2 methyl of (ScNsrR) Thr41 (Table 2). Because the latter is located in the N-terminal region of the RH and its O γ 1 atom makes a H-bond with the 5'-phosphate group of the same base in *hmpA1* (Table S1), other interactions involving the RH are likely to be perturbed as well. The same substitution in the other DNA strand should similarly modify the RH of the corresponding ScNsrR subunit, which could be sufficient to abolish binding. Similarly, when modeled on the structure of *hyA*,

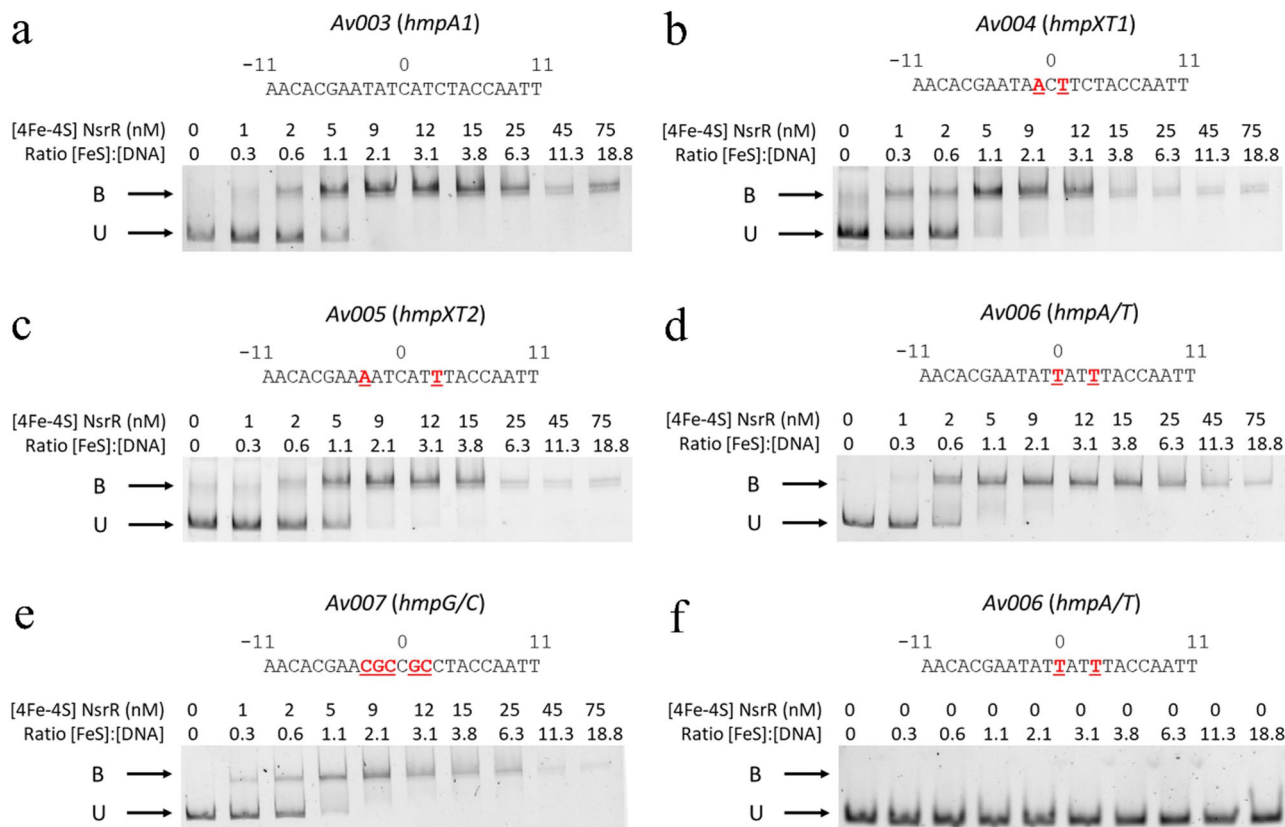


Fig. 7 Binding of NsrR to modified probes. DNA binding EMSAs showing probes (Av003 – Av007) unbound (U) or bound (B) by [4Fe-4S] NsrR. Probes contain: **a** Wild type *hmpA1* operator, **b** *hmpXT1*, **c** *hmpXT2*, **d** *hmpA/T*, **e** *hmpG/C* sequences, **f** Protein-free control for *hmpA/T*. Base sequences for each probe are shown, with changes relative to the wild type *hmpA1* site shown in red. The DNA concentration was ~ 4 nM. Concentration of [4Fe-4S] NsrR used and ratios of [4Fe-4S] NsrR to DNA are indicated. The binding buffer contained 10 mM Tris, 54 mM KCl, 0.3% (v/v) glycerol, 1.32 mM GSH, pH 7.5.

the C7 methyl group of T_{+5} found in one strand of *hmpA1* and in both strands of *rsrR* lies within 2 Å from the side chain of Ser40 of *EcIscR* (Table 2). In addition, the T_{-8d} C7 methyl group of *hmpA1* would collide with the carboxylate group of *EcIscR* Glu43, which has been assigned an important role in DNA recognition¹⁷. These collisions suggest that *hmpA1* and *rsrR* are not recognized by *EcIscR*. Because of its relatively low resolution²¹, we refrained from doing a similar analysis using the structure of the *SvRsrR/rsrR* complex.

The observed interaction of Pro61 in the wing of *EcIscR* with the MiG of a 29 bp fragment of *hyA* (Table S1) suggests that the aligned Arg62 of ScNsrR could bind to the MiG of a longer than 23 bp fragment of *hmpA1*, as the one used in our EMSA studies which is 151 bp-long (Fig. 7). This should increase binding affinity. Substitution of (*hmpA1*) T_{+10} by (*rsrR*) G_{+10} introduces vdW collisions with (ScNsrR) Arg60 in both wing regions (Table 2). We also noted that the last three Gly residues of the conserved $Lx_3Gx_6Gx_2GGx_2L$ wing motif directly interact with the DNA in the *EcIscR/hyA* complex structure (Table S1). This further underscores the importance of the wing region for DNA binding.

There are few structural changes in [4Fe-4S]-ScNsrR upon its binding to the *hmpA1* operator (Fig. 4a). As mentioned in the Introduction, the *nsrR* gene codes for ScNsrR, whereas the two *hmpA* genes encode NO-detoxifying flavohemoglobins. Full binding of the [4Fe-4S]-ScNsrR dimer to 23 bp DNA stretches -included near the center of 267 bp constructs- as investigated by earlier reported EMSA studies²⁵, requires corresponding ratios of 1:1 for *hmpA1*, 2.5:1 for *nsrR* and 4:1 for *hmpA2*. NO-induced structural changes resulting from iron-sulfur cluster modification and degradation will alter the ScNsrR structure and,

consequently, modify its binding affinity. The [4Fe-4S]-ScNsrR TF binds to its known operators²⁵ with much higher affinity than either non-physiological [2Fe-2S]-ScNsrR species²⁹ or its apo-form. We have provided structural data to show that the loss of the iron-sulfur cluster in the latter introduces radical structural differences relative to the holo protein form at the DNA-interacting region²². Large conformational changes, including the possible formation of persulfide bonds²⁷, should also be present in [2Fe-2S]-ScNsrR; indeed these bonds have been observed in partially oxidized [2Fe-2S] clusters of HydE⁵² and detected by resonance Raman spectroscopy in FNR⁵³.

We have found that the DNA-free [4Fe-4S]-ScNsrR structure does not change much after binding of the 23 bp *hmpA1* operator fragment and that changing the sequence of its central 7-bp region (which shows no direct base-protein contacts within 4 Å) has no effect on the binding affinity. Consequently, it seems reasonable to assume that the DNA backbone conformation of bound *hmpA2* and *nsrR* operators is not very different from that of *hmpA1*. We have therefore modeled the *hmpA2*, *nsrR* and (*Ec*) *hmpA* sequences on that of *hmpA1*, knowing that (*Ec*) *hmpA* binds only very weakly to ScNsrR²⁵. Analysis of the resulting predicted complex structures shows a number of bad contacts involving Arg60 in the two NsrR wing regions. Together, pointing into the minor groove at the two extremes of the *hmpA1* operator fragment, Arg60_A and Arg60_B make close (< 4 Å) contacts with eleven nucleotides (Fig. 2 and Table S1). A collision with one of these nucleotides should perturb the interactions with the other ones. Three bad ($d < 2.85$ Å) vdW contacts with Arg60 are obtained for the modeled ScNsrR/*Ec-hmpA* complex (Tables S3–S4 and Fig. S12), which could explain why no significant binding is observed for this operator. One bad contact with the Arg60

guanidinium group is obtained for *nsrR*, in line with its reduced binding affinity. The observed low affinity of *hmpA2* is possibly explained by the substitution of T_{-9d} by C and T_{+5d} by G causing a loss of favorable vdW contacts with the T-C7 methyl groups.

Holo-ScNsrR-operator binding is abolished for NO-to-[4Fe-4S]-cluster ratios of about 2 for *hmpA2*, 4 for *hmpA1* and 8 for *nsrR*²⁴. As in the case of O₂ oxidation, important conformational changes at the cluster region are expected when intermediate NO-bound degradation products are formed. Kinetic and spectroscopic studies have shown that these intermediates appear at ratios of about 2, 4, and 6 bound NOs per cluster²⁴. They share spectral features with known NO-iron complexes such as [Fe(NO)₂(RS)₂] (dinitrosyl iron complex), [Fe₂(NO)₄(RS)₂] (Roussin's red ester) and [Fe₄(NO)₇(S)₃] (Roussin's black salt, RBS)^{24,26}. In the case of the RBS-like intermediate, it has been suggested that Cys thiolates (or persulfide derivatives of these) replace sulfide ligands^{26,28}; this would explain how these nitrosylated moieties bind to the protein after the loss of cluster sulfide ions. Several NO-modified cluster forms have also been characterized by mass spectrometry, including early mono- and di-nitrosyl intermediates of the [4Fe-4S] cluster²⁸. At higher NO-to-cluster ratios, persulfide adducts accumulate, with a gradual breakdown of the [4Fe-4S] core to form [Fe₂(NO)₄] and [Fe₂(NO)₄S] adducts²⁷. The ScNsrR-*hmpA1* complex starts to dissociate at ~2 NO per [4Fe-4S] cluster, where only early intermediates of nitrosylation are observed. This suggests that relatively minor modifications of the cluster can abolish operator binding. The comparison of both non-complexed and complexed [4Fe-4S]-ScNsrR to apo-ScNsrR²² has defined the nature of the conformational changes induced by either iron-sulfur cluster modification or loss that will preclude sensor binding to *hmpA1* (Fig. 4b). Because we have not yet characterized any NO-complex of ScNsrR, we have at this stage no structural data to explain the different NO sensitivities of its complexes with *hmpA2*, *hmpA1* and *nsrR*.

In conclusion, the main determinant factors for the ScNsrR base sequence specificity can be described as follows: (i) the end regions of the *hmpA1* operator interact extensively with the ScNsrR wings (this is also the case for *hya* and *rsrR*, which respectively bind the apo-*EclsrR* and [2Fe-2S]-*SvRsrR* wings); (ii) important structural differences between the bound operators of these three Rrf2 family members reside in variations of minor and major groove widths, which result in different phosphate positions; (iii) the DNA also displays specific curvatures around the RH of the sensor that properly orient its phosphate groups to form salt bridges and hydrogen bonds with equivalent side chains from both protein subunits; (iv) much of the specificity involves a relatively small number of direct interactions of protein side chains with nucleobase rings; (v) as shown in the EMSA experiments, changes in the flexibility of the *hmpA1* central region do not affect the thermodynamics of NsrR binding (whether they modify the kinetics of this process was not investigated here). Solvent-mediated interactions may also play a role, but these are not resolved in our 3 Å resolution X-ray model. Our results extend the findings of a recently reported sequence similarity network analysis of the entire Rrf2 superfamily that places ScNsrR, *EcNsrR*, *EclsrR* and *SvRsrR* in distinct cluster configurations⁵⁴. Our next challenges will be to crystallize complexes of [4Fe-4S]-ScNsrR with longer constructs of the *hmpA1*, *hmpA2* and *nsrR* operators and solve their structures at the highest possible resolution. These structures should help us determine if and how the above-described determinants vary with the nature of the operator. In addition, we aim now at structurally characterizing NO-induced changes for at least one ScNsrR/DNA complex.

Methods

Crystallization. [4Fe-4S]-ScNsrR was purified under strictly anaerobic conditions as described previously^{22,25}. A stock solution with a protein concentration of 43 mg/mL in 50 mM Tris pH 8.0, 2 M NaCl, 5% glycerol was used for all

experiments. A 23 bp dsDNA fragment of the *hmpA1* operator was prepared by annealing its 5'-AACACGAATATCATCTACCAATT-3' and 5'-AATTGGTA-GATGATATTCGTGTT-3' complementary oligonucleotides in DNase-free water (Alfa Aesar), as already described previously²⁴. [4Fe-4S]-ScNsrR was complexed with the 23 bp *hmpA1* operator by incubating a solution of 17 mg/mL of the protein mixed with a 3-fold excess of the dsDNA fragment in 50 mM Tris pH 8.0, 500 mM NaCl, 5% glycerol for 60 minutes at 20 °C. Crystals were obtained by screening 864 different conditions from commercial kits in 96-well plates with a Gryphon robot (Art Robbins Instruments, CA, USA) installed inside an anaerobic glove box, using the vapor diffusion method. For each crystallization condition a drop was set by the robot by mixing 200 nL of the solution of the [4Fe-4S]-ScNsrR/*hmpA1* complex with 200 nL of the commercial reservoir solution. The sitting drop was then equilibrated against 100 μL of the latter solution. Manual optimization of the best automated crystallization condition yielded usable crystals from hanging drops prepared by mixing 1 μL of the protein-DNA mix with 1 μL of the reservoir solution containing 27% PEG 550 MME, 13.5% PEG 20000, 30 mM MgCl₂, 30 mM CaCl₂ and 100 mM MOPS/HEPES pH 8.0 equilibrated against 1 mL of this solution. All these experiments were performed anaerobically in a glove box.

X-ray data collection. Crystals were transferred from the original drop to the crystallization solution, with or without 20% v/v glycerol added as cryoprotectant. They were then fished with a cryo-loop, flash-cooled in liquid propane inside the glove box⁵⁵ and transferred outside for storage in liquid nitrogen. Initial X-ray diffraction data were collected to 4.1 Å resolution for a crystal mounted from a cryo-protected solution, while maintaining it under a N₂ stream at 100 K at beamline PX-2A of the SOLEIL synchrotron (Saint-Aubain, France). Data to about 3.0 Å resolution were subsequently obtained from crystals flash-cooled without added glycerol. The best data set (Table 1) was collected at a temperature of 100 K and a wavelength of 1.00001 Å with an Eiger X 9 M (Dectris) detector at beamline X06SA of the Swiss Light Source (Villigen, Switzerland), using the DA+ software⁵⁶. The diffraction data were indexed, integrated and scaled with the XDS package⁵⁷ and the program AIMLESS⁵⁸ was used to check for anisotropic diffraction. Although X-ray data reduction initially indicated that the crystal belonged to the hexagonal P6₅22 space group, further analysis showed it to be P6₅. The change in Laue class from 6/mmm to 6/m of the diffraction data set results from the fact that the dsDNA fragment is not a perfect palindrome; consequently, it does not display the twofold symmetry of the protein dimer. The intensity statistics of the data showed no evidence of twinning.

Structure determination. The structure of the [4Fe-4S]-ScNsrR/*hmpA1* complex was solved by molecular replacement (MR) with PHASER⁵⁹ using two search models: the known non-complexed protein structure²² and the 23 bp *hmpA1* operator. The latter was constructed with B-DNA geometry using COOT⁶⁰. The obtained MR solutions were confirmed by high peaks in F_{obs}-F_{calc} and anomalous difference electron density maps for the ScNsrR [4Fe-4S] clusters, which were not included in the protein search model. The resulting model was subjected to rigid body, positional, TLS and B-factor refinement with the PHENIX and Refmac5 programs^{61,62}, using COOT⁶⁰ for manual corrections. Non-crystallographic symmetry and secondary structure restraints were used for positional refinement. H-bond restraints were included for DNA base pairing interactions and some protein-DNA contacts. The refinement procedure gave best results when defining the *hmpA1* 23 bp operator and two protein half-dimers as TLS groups. No hydrogens were included in the model. Each half-dimer consisted of NsrR residues 1–86 and 124–144 from one subunit and residues 87–123 from the other, including also the [4Fe-4S] cluster bound between them. The final model has good refinement statistics, stereochemistry (Table 1) and a low all-atom clash score of 3.8, as measured by MolProbity⁶³. There are 0 outliers in the Ramachandran (ϕ-ψ) plot and 2.3% rotamer outliers. The dsDNA fragment fits well to the electron density map but a relatively poor match is observed for about 30% of the protein model due to disorder, as indicated by high B-factors. However, all ScNsrR side chains forming hydrogen bonds or salt bridges with the dsDNA have good matching electron density. We tried to explain residual peaks found at both ends of the *hmpA1* operator fragment in the final F_{obs}-F_{calc} map by adding additional ordered nucleotides to the model. However, this resulted in an increase of the R_{free}. Because a threefold excess of DNA was used for crystallization, we tentatively assign these residual peaks to partially disordered non-complexed DNA. Other operator sequences were modeled with COOT⁶⁰ on the available structures of *hmpA1* (this study) and *hya*¹⁷ without changing the structure of the DNA backbone.

Structural analyses. Buried surface areas (BSAs) between the various protein and DNA chains were determined with the program Pisa⁶⁴. DNA geometry, including the measurement of torsion angles, bp origins, rolls and propeller twists, was analyzed with DSSR³⁷, with groove widths calculated from phosphate-P positions as defined by El Hassan & Calladine⁶⁵ (Fig. S10). We also used the in-house program CavEnv (incorporated in the CCP4 package⁶⁶), which takes into account all atoms of the structure with an atom-type dependent vdW radius, to investigate cavities and groove widths (Fig. S7). Figures were prepared with either COOT⁶⁰, Bobscrip⁶⁷ and Raster3D⁶⁸, PyMOL (www.pymol.org, the PyMOL molecular graphics system, version 2.1 Schrödinger, LLC) or manually. Compilations of all

the used programs were provided by SBGrid⁶⁹. The A/T notation for bps and AT for base steps is used throughout, with a number and one letter for the strand added as an index in some cases. Nucleotides are numbered with respect to the central bp, which is assigned the value zero. Amino acid residues are shown using three-letter codes in the text and one-letter codes in the figures and tables. Structures of the *Ec*IscR/*hya* and *Sv*RsrR/*rsrR* complexes were obtained from deposition codes 4HF1 and 6Y42 in the Protein Data Bank⁷⁰.

EMSA (electrophoretic mobility shift assay) binding studies. DNA fragments carrying wild type or mutated *hmpA1* promoter sequences (Table S2) were PCR-amplified using a 151-base-pair double-stranded DNA template, 6-carboxyfluorescein (6-FAM) modified primers (Metabion, Germany) and Phusion Hot Start II DNA Polymerase (Thermo Scientific). The PCR products were purified using NucleoSpin Gel and PCR Clean-up kit (Macherey-Nagel) according to the manufacturer's instructions. The concentration of the 6-FAM labeled probes was determined using a Varian Cary 50 UV-Vis spectrophotometer. The molecular weights and 260 nm absorption coefficients for 6-FAM labeled probes were calculated using OligoCalc⁷¹. EMSA reactions (20 μ l) were carried out on ice in 10 mM Tris, 54 mM KCl, 0.3% (v/v) glycerol, 1.32 mM glutathione, pH 7.5, as previously described²⁵. Briefly, 2 μ l of each DNA probe was titrated with varying aliquots of [4Fe-4S] NsrR, to a ~20-fold molar excess. Loading dye (2 μ l of 0.3% (w/v) bromophenol blue, 50% (w/v) glycerol) was added and the reaction mixtures were immediately separated at 30 mA for 30 min on a 5% (w/v) polyacrylamide gel in 1 \times TBE (89 mM Tris, 89 mM boric acid, 2 mM EDTA). Gels were visualized on a Typhoon FLA9000 (GE Healthcare). Polyacrylamide gels were pre-run at 30 mA for 2 min prior to use. Each probe has a dimeric NsrR binding site with one [4Fe-4S] cluster per protein subunit. As apo-NsrR does not bind DNA²⁵, concentrations are presented as [4Fe-4S] per DNA, as indicated in Fig. 7.

Statistics and reproducibility. X-ray diffraction data collection and refinement statistics for the reported NsrR/*hmpA1* complex are given in Table 1. EMSAs for each tested DNA fragment were carried out at least twice, on different days, to ensure repeatable observations. The images shown in Fig. 7 are the best representative images for each EMSA probe.

Reporting summary. Further information on research design is available in the Nature Research Reporting Summary linked to this article.

Data availability

Atomic coordinates and structure factors for the reported crystal structure have been deposited with the Protein Data Bank⁷⁰ (<https://www.rcsb.org>) under accession number 7B0C. A structure validation report is also available there. The two other structures used in our paper are available in the Protein Data Bank (pdb) under accession codes 4HF1 and 6Y42, as given in Fig. 5. These pdb depositions were used to generate all the figures given in the main manuscript, as stated above in the section Structural Analyses, except for the manually prepared Fig. 5 and the measured EMSAs in Fig. 7. For the latter, uncropped images are included in the Supplementary Material as Fig. S13. Interatomic distances in Figs. 1–3, 6b, and c were measured from the atomic coordinates in the pdb depositions given above. Amino acid sequences in Fig. 5 were obtained from the pdb deposition codes mentioned in its last column or from the UniProt database (<https://www.uniprot.org>, codes Q1R382 for *Ec*NsrR and Q1ML82 for *R*RirA).

Received: 9 April 2021; Accepted: 21 July 2022;

Published online: 30 July 2022

References

- Browning, D. F. & Busby, S. J. The regulation of bacterial transcription initiation. *Nat. Rev. Microbiol.* **2**, 57–65 (2004).
- Browning, D. F. & Busby, S. J. W. Local and global regulation of transcription initiation in bacteria. *Nat. Rev. Microbiol.* **14**, 638–650 (2016).
- Kiley, P. J. & Beinert, H. Oxygen sensing by the global regulator, FNR: the role of the iron-sulfur cluster. *FEMS Microbiol. Rev.* **22**, 341–352 (1998).
- Yukl, E. T., Elbaz, M. A., Nakano, M. M. & Moëne-Loccoz, P. Transcription Factor NsrR from *Bacillus subtilis* Senses Nitric Oxide with a 4Fe-4S Cluster. *Biochemistry* **47**, 13084–13092 (2008).
- Munnich, J. T. et al. Characterization of a putative NsrR homologue in *Streptomyces venezuelae* reveals a new member of the Rrf2 superfamily. *Sci. Rep.* **6**, 31597 (2016).
- Giel, J. L. et al. Regulation of iron-sulphur cluster homeostasis through transcriptional control of the Isc pathway by [2Fe-2S]-IscR in *Escherichia coli*. *Mol. Microbiol.* **87**, 478–492 (2013).
- Pellicer Martinez, M. T. et al. Sensing iron availability via the fragile [4Fe-4S] cluster of the bacterial transcriptional repressor RirA. *Chem. Sci.* **8**, 8451–8463 (2017).
- Volbeda, A., Darnault, C., Renoux, O., Nicolet, Y. & Fontecilla-Camps, J. C. The crystal structure of the global anaerobic transcriptional regulator FNR explains its extremely fine-tuned monomer-dimer equilibrium. *Sci. Adv.* **1**, e1501086 (2015).
- Lazizzera, B. A., Bates, D. M. & Kiley, P. J. The activity of the *Escherichia coli* transcription factor FNR is regulated by a change in oligomeric state. *Genes Dev.* **7**, 1993–2005 (1993).
- Keon, R. G., Fu, R. & Voordouw, G. Deletion of two downstream genes alters expression of the hmc operon of *Desulfovibrio vulgaris* subsp. *vulgaris* Hildenborough. *Arch. Microbiol.* **167**, 376–383 (1997).
- Shepard, W. et al. Insights into the Rrf2 repressor family—the structure of CymR, the global cysteine regulator of *Bacillus subtilis*. *FEBS J.* **278**, 2689–2701 (2011).
- Ji, Q. et al. *Staphylococcus aureus* CymR is a new thiol-based oxidation-sensing regulator of stress resistance and oxidative response. *J. Biol. Chem.* **287**, 21102–21109 (2012).
- Tanous, C. et al. The CymR regulator in complex with the enzyme CysK controls cysteine metabolism in *Bacillus subtilis*. *J. Biol. Chem.* **283**, 35551–35560 (2008).
- Santos, J. A., Pereira, P. J. B. & Macedo-Ribeiro, S. What a difference a cluster makes: The multifaceted roles of IscR in gene regulation and DNA recognition. *Biochim. Biophys. Acta BBA - Proteins Proteom.* **1854**, 1101–1112 (2015).
- Pellicer Martinez, M. T. et al. Mechanisms of iron- and O₂-sensing by the [4Fe-4S] cluster of the global iron regulator RirA. *eLife* **8**, e47804 (2019).
- Tucker, N. P., Le Brun, N. E., Dixon, R. & Hutchings, M. I. There's NO stopping NsrR, a global regulator of the bacterial NO stress response. *Trends Microbiol.* **18**, 149–156 (2010).
- Rajagopalan, S. et al. Studies of IscR reveal a unique mechanism for metal-dependent regulation of DNA binding specificity. *Nat. Struct. Mol. Biol.* **20**, 740–747 (2013).
- Santos, J. A., Alonso-García, N., Macedo-Ribeiro, S. & Pereira, P. J. B. The unique regulation of iron-sulfur cluster biogenesis in a Gram-positive bacterium. *Proc. Natl. Acad. Sci. USA* **111**, E2251–E2260 (2014).
- Nesbit, A. D., Giel, J. L., Rose, J. C. & Kiley, P. J. Sequence-specific binding to a subset of IscR-regulated promoters does not require IscR Fe-S cluster ligation. *J. Mol. Biol.* **387**, 28–41 (2009).
- Volbeda, A. et al. Crystal Structure of the Transcription Regulator RsrR Reveals a [2Fe-2S] Cluster Coordinated by Cys, Glu, and His Residues. *J. Am. Chem. Soc.* **141**, 2367–2375 (2019).
- Crack, J. C. et al. Electron and Proton Transfers Modulate DNA Binding by the Transcription Regulator RsrR. *J. Am. Chem. Soc.* **142**, 5104–5116 (2020).
- Volbeda, A. et al. Crystal structures of the NO sensor NsrR reveal how its iron-sulfur cluster modulates DNA binding. *Nat. Commun.* **8**, 15052 (2017).
- Stevanin, T. M., Read, R. C. & Poole, R. K. The *hmp* gene encoding the NO-inducible flavohaemoglobin in *Escherichia coli* confers a protective advantage in resisting killing within macrophages, but not in vitro: links with swarming motility. *Gene* **398**, 62–68 (2007).
- Crack, J. C. et al. Differentiated, Promoter-specific Response of [4Fe-4S] NsrR DNA Binding to Reaction with Nitric Oxide. *J. Biol. Chem.* **291**, 8663–8672 (2016).
- Crack, J. C. et al. NsrR from *Streptomyces coelicolor* is a nitric oxide-sensing [4Fe-4S] cluster protein with a specialized regulatory function. *J. Biol. Chem.* **290**, 12689–12704 (2015).
- Serrano, P. N. et al. Nitrosylation of Nitric-Oxide-Sensing Regulatory Proteins Containing [4Fe-4S] Clusters Gives Rise to Multiple Iron-Nitrosyl Complexes. *Angew. Chem. Int. Ed Engl.* **55**, 14575–14579 (2016).
- Crack, J. C., Hamilton, C. J. & Le Brun, N. E. Mass spectrometric detection of iron nitrosyls, sulfide oxidation and mycothiolation during nitrosylation of the NO sensor [4Fe-4S] NsrR. *Chem. Commun. Camb. Engl.* **54**, 5992–5995 (2018).
- Crack, J. C. & Le Brun, N. E. Mass Spectrometric Identification of [4Fe-4S] (NO)_x Intermediates of Nitric Oxide Sensing by Regulatory Iron-Sulfur Cluster Proteins. *Chem. Weinh. Bergstr. Ger.* **25**, 3675–3684 (2019).
- Tucker, N. P. et al. The transcriptional repressor protein NsrR senses nitric oxide directly via a [2Fe-2S] cluster. *PLoS One* **3**, e3623 (2008).
- Partridge, J. D., Bodenmiller, D. M., Humphrys, M. S. & Spiro, S. NsrR targets in the *Escherichia coli* genome: new insights into DNA sequence requirements for binding and a role for NsrR in the regulation of motility. *Mol. Microbiol.* **73**, 680–694 (2009).
- Karlinsky, J. E. et al. The NsrR regulon in nitrosative stress resistance of *Salmonella enterica* serovar Typhimurium. *Mol. Microbiol.* **85**, 1179–1193 (2012).
- Rohs, R. et al. Origins of specificity in protein-DNA recognition. *Annu. Rev. Biochem.* **79**, 233–269 (2010).
- Slattery, M. et al. Absence of a simple code: how transcription factors read the genome. *Trends Biochem. Sci.* **39**, 381–399 (2014).

34. Fratini, A. V., Kopka, M. L., Drew, H. R. & Dickerson, R. E. Reversible bending and helix geometry in a B-DNA dodecamer: CGCGAATTBrCGCG. *J. Biol. Chem.* **257**, 14686–14707 (1982).
35. Heddi, B., Foloppe, N., Bouchemal, N., Hantz, E. & Hartmann, B. Quantification of DNA BI/BII backbone states in solution. Implications for DNA overall structure and recognition. *J. Am. Chem. Soc.* **128**, 9170–9177 (2006).
36. Aravind, L., Anantharaman, V., Balaji, S., Babu, M. M. & Iyer, L. M. The many faces of the helix-turn-helix domain: transcription regulation and beyond. *FEMS Microbiol. Rev.* **29**, 231–262 (2005).
37. Lu, X.-J., Bussemaker, H. J. & Olson, W. K. DSSR: an integrated software tool for dissecting the spatial structure of RNA. *Nucleic Acids Res.* **43**, e142 (2015).
38. Liebl, K. & Zacharias, M. How methyl-sugar interactions determine DNA structure and flexibility. *Nucleic Acids Res.* **47**, 1132–1140 (2019).
39. Travers, A. A. The structural basis of DNA flexibility. *Philos. Trans. R. Soc. -Math. Phys. Eng. Sci.* **362**, 1423–1438 (2004).
40. Bothe, J. R., Lowenhaupt, K. & Al-Hashimi, H. M. Sequence-Specific B-DNA Flexibility Modulates Z-DNA Formation. *J. Am. Chem. Soc.* **133**, 2016–2018 (2011).
41. Johnson, S., Chen, Y.-J. & Phillips, R. Poly(dA:dT)-Rich DNAs Are Highly Flexible in the Context of DNA Looping. *PLoS One* **8**, e75799 (2013).
42. Wang, Y. M., Austin, R. H. & Cox, E. C. Single molecule measurements of repressor protein 1D diffusion on DNA. *Phys. Rev. Lett.* **97**, 048302 (2006).
43. Sakata-Sogawa, K. & Shimamoto, N. RNA polymerase can track a DNA groove during promoter search. *Proc. Natl. Acad. Sci. USA* **101**, 14731–14735 (2004).
44. Privalov, P. L., Dragan, A. I. & Crane-Robinson, C. Interpreting protein/DNA interactions: distinguishing specific from non-specific and electrostatic from non-electrostatic components. *Nucleic Acids Res.* **39**, 2483–2491 (2011).
45. Redding, S. & Greene, E. C. How do proteins locate specific targets in DNA? *Chem. Phys. Lett.* **570**, 1–11 (2013).
46. Stella, S., Cascio, D. & Johnson, R. C. The shape of the DNA minor groove directs binding by the DNA-bending protein Fis. *Genes Dev.* **24**, 814–826 (2010).
47. Hizver, J., Rozenberg, H., Frolow, F., Rabinovich, D. & Shakked, Z. DNA bending by an adenine-thymine tract and its role in gene regulation. *Proc. Natl. Acad. Sci. USA* **98**, 8490–8495 (2001).
48. Lu, X.-J. & Olson, W. K. 3DNA: A versatile, integrated software system for the analysis, rebuilding and visualization of three-dimensional nucleic-acid structures. *Nat. Protoc.* **3**, 1213–1227 (2008).
49. Heddi, B., Oguey, C., Lavelle, C., Foloppe, N. & Hartmann, B. Intrinsic flexibility of B-DNA: The experimental TRX scale. *Nucleic Acids Res.* **38**, 1034–1047 (2010).
50. Mack, D. R., Chiu, T. K. & Dickerson, R. E. Intrinsic bending and deformability at the T-A step of CCTTTAAAGG: a comparative analysis of T-A and A-T steps within A-tracts. *J. Mol. Biol.* **312**, 1037–1049 (2001).
51. Yella, V. R. et al. Flexibility and structure of flanking DNA impact transcription factor affinity for its core motif. *Nucleic Acids Res.* **46**, 11883–11897 (2018).
52. Nicolet, Y., Rohac, R., Martin, L. & Fontecilla-Camps, J. C. X-ray snapshots of possible intermediates in the time course of synthesis and degradation of protein-bound Fe₄S₄ clusters. *Proc. Natl. Acad. Sci. USA* **110**, 7188–7192 (2013).
53. Zhang, B. et al. Reversible cycling between cysteine persulfide-ligated [2Fe-2S] and cysteine-ligated [4Fe-4S] clusters in the FNR regulatory protein. *Proc. Natl. Acad. Sci. USA* **109**, 15734–15739 (2012).
54. Zhang, Y., Martin, J. E., Edmonds, K. A., Winkler, M. E. & Giedroc, D. P. SifR is an Rrf2-family quinone sensor associated with catechol iron uptake in *Streptococcus pneumoniae* D39. *J. Biol. Chem.* **298**, 102046 (2022).
55. Vernede, X. & Fontecilla-Camps, J. C. A method to stabilize reduced and or gas-treated protein crystals by flash-cooling under a controlled atmosphere. *J. Appl. Crystallogr.* **32**, 505–509 (1999).
56. Wojdyła, J. A. et al. DA+ data acquisition and analysis software at the Swiss Light Source macromolecular crystallography beamlines. *J. Synchrotron Radiat.* **25**, 293–303 (2018).
57. Kabsch, W. XDS. *Acta Crystallogr. D. Biol. Crystallogr.* **66**, 125–132 (2010).
58. Evans, P. R. & Murshudov, G. N. How good are my data and what is the resolution? *Acta Crystallogr. D. Biol. Crystallogr.* **69**, 1204–1214 (2013).
59. McCoy, A. J. et al. Phaser crystallographic software. *J. Appl. Crystallogr.* **40**, 658–674 (2007).
60. Emsley, P., Lohkamp, B., Scott, W. G. & Cowtan, K. Features and development of Coot. *Acta Crystallogr. D. Biol. Crystallogr.* **66**, 486–501 (2010).
61. Adams, P. D. et al. PHENIX: A comprehensive Python-based system for macromolecular structure solution. *Acta Crystallogr. D. Biol. Crystallogr.* **66**, 213–221 (2010).
62. Murshudov, G. N. et al. REFMAC5 for the refinement of macromolecular crystal structures. *Acta Crystallogr. D. Biol. Crystallogr.* **67**, 355–367 (2011).
63. Williams, C. J. et al. MolProbity: More and better reference data for improved all-atom structure validation. *Protein Sci. Publ. Protein Soc.* **27**, 293–315 (2018).
64. Krissinel, E. & Henrick, K. Inference of macromolecular assemblies from crystalline state. *J. Mol. Biol.* **372**, 774–797 (2007).
65. El Hassan, M. A. & Calladine, C. R. Two distinct modes of protein-induced bending in DNA. *J. Mol. Biol.* **282**, 331–343 (1998).
66. Winn, M. D. et al. Overview of the CCP4 suite and current developments. *Acta Crystallogr. D. Biol. Crystallogr.* **67**, 235–242 (2011).
67. Esnouf, R. M. Further additions to MolScript version 1.4, including reading and contouring of electron-density maps. *Acta Crystallogr. D. Biol. Crystallogr.* **55**, 938–940 (1999).
68. Merritt, E. A. & Murphy, M. E. Raster3D Version 2.0. A program for photorealistic molecular graphics. *Acta Crystallogr. D. Biol. Crystallogr.* **50**, 869–873 (1994).
69. Morin, A. et al. Collaboration gets the most out of software. *eLife* **2**, e01456 (2013).
70. Berman, H. M. et al. The Protein Data Bank. *Nucleic Acids Res.* **28**, 235–242 (2000).
71. Kibbe, W. A. OligoCalc: An online oligonucleotide properties calculator. *Nucleic Acids Res.* **35**, W43–W46 (2007).

Acknowledgements

We thank Christophe Caillat for collecting the first ScNsrR/hmpA1 complex X-ray diffraction data set at the SOLEIL synchrotron. We acknowledge the Paul Scherrer Institut, Villigen, Switzerland for provision of synchrotron radiation beamtime at beamline X06SA of the SLS and thank Ezequiel Panepucci for assistance with data collection. This work was supported by the Agence Nationale de la Recherche [ANR-18-CE11-0010 (MANGO-ICING) and ANR-10-INSB-05-02 (FRISBI, within the Grenoble Partnership for Structural Biology)], the European Union's Horizon 2020 Research and Innovation programme [grant agreement nr. 730872 (CALIPSOplus)] and the Biotechnology and Biological Sciences Research Council [BB/P006140/1]. Funding for open charge access: [ANR-18-CE11-0010].

Author contributions

R.R., J.C.C., E.d.R., N.E.L.B., J.C.F.-C., and A.V. designed the experiments, R.R., J.C.C., O.G., and A.V. performed the experiments, R.R., J.C.C., E.d.R., N.E.L.B., J.C.F.-C., and A.V. wrote the paper.

Competing interests

The authors declare no competing interests.

Additional information

Supplementary information The online version contains supplementary material available at <https://doi.org/10.1038/s42003-022-03745-7>.

Correspondence and requests for materials should be addressed to Anne Volbeda.

Peer review information *Communications Biology* thanks Hideaki Ogata and the other, anonymous, reviewer(s) for their contribution to the peer review of this work. Primary Handling Editors: Ingrid Span and Eve Rogers.

Reprints and permission information is available at <http://www.nature.com/reprints>

Publisher's note Springer Nature remains neutral with regard to jurisdictional claims in published maps and institutional affiliations.

 **Open Access** This article is licensed under a Creative Commons Attribution 4.0 International License, which permits use, sharing, adaptation, distribution and reproduction in any medium or format, as long as you give appropriate credit to the original author(s) and the source, provide a link to the Creative Commons license, and indicate if changes were made. The images or other third party material in this article are included in the article's Creative Commons license, unless indicated otherwise in a credit line to the material. If material is not included in the article's Creative Commons license and your intended use is not permitted by statutory regulation or exceeds the permitted use, you will need to obtain permission directly from the copyright holder. To view a copy of this license, visit <http://creativecommons.org/licenses/by/4.0/>.

© The Author(s) 2022